Location of the Zn^{2+}-Binding Site on S100B As Determined by NMR Spectroscopy and Site-Directed Mutagenesis†

Paul T. Wilder,‡ Donna M. Baldisseri,§ Ryan Udan,§ Kristen M. Vallely,‡ and David J. Weber*,‡,§

Molecular and Cell Biology Program and Department of Biochemistry and Molecular Biology, University of Maryland School of Medicine, 108 North Greene Street, Baltimore, Maryland 21201

Received July 28, 2003; Revised Manuscript Received September 23, 2003

ABSTRACT: In addition to binding Ca^{2+}, the S100 protein S100B binds Zn^{2+} with relatively high affinity as confirmed using isothermal titration calorimetry (ITC; $K_d = 94 \pm 17$ nM). The Zn^{2+}-binding site on Ca^{2+}-bound S100B was examined further using NMR spectroscopy and site-directed mutagenesis. Specifically, ITC measurements of S100B mutants (helix 1, H15A and H25A; helix 4, C84A, H85A, and H90A) were found to bind Zn^{2+} with lower affinity than wild-type S100B (from 2- to >25-fold). Thus, His-15, His-25, Cys-84, His-85, and perhaps His-90 of S100B are involved in coordinating Zn^{2+}, which was confirmed by NMR spectroscopy. Previous studies indicate that the binding of Zn^{2+} enhances calcium and target protein-binding affinities, which may contribute to its biological function. Thus, chemical shift perturbations observed here for residues in both EF-hand domains of S100B during Zn^{2+} titrations could be detecting structural changes in the Ca^{2+}-binding domains of S100B that are pertinent to its increase in Ca^{2+}-binding affinity in the presence of Zn^{2+}. Furthermore, Zn^{2+} binding causes helix 4 to extend by one full turn when compared to Ca^{2+}-bound S100B. This change in secondary structure likely contributes to the increased binding affinity that S100B has for target peptides (i.e., TRTK peptide) in the presence of Zn^{2+}.

S100B is a Ca^{2+}-binding protein involved in the regulation of cell growth and differentiation and is overexpressed in Alzheimer's disease, Down's syndrome, and several forms of cancer (*1*, *2*). Like other EF-hand-containing proteins, S100B undergoes a Ca^{2+}-dependent conformational change that is necessary for it to interact with a variety of protein targets inside the cell and regulate their biological function (*2*, *3*). For example, binding of S100B to GFAP[1] (*4*) and microtubules (*5*) inhibits their assembly and thus regulates the biological function of these protein targets. S100B also inhibits the PKC-dependent phosphorylation of p53 (*6*), Tau (*7*), GAP-43 (*8*), and MARCKS (*9*) in a Ca^{2+}-dependent manner by sterically blocking the phosphorylation sites of these PKC substrates upon binding. In the case of p53, the Ca^{2+}-dependent interaction with S100B also dissociates the p53 tetramer (*10*, *11*) and inhibits its transcriptional activation activity necessary for tumor suppression function (*12*).

In addition to binding calcium, S100 proteins, such as S100B, also bind Zn^{2+} at a site distinct from the EF-hand calcium-binding domains. In most cases, the binding of Zn^{2+} affects Ca^{2+}-binding and target protein-binding affinities of the S100 protein. For example, Zn^{2+} binds S100B with relatively high affinity (~100 nM) (*13*, *14*), and the affinity of Ca^{2+} for S100B increases by as much as 10-fold in the presence of Zn^{2+} (*15*). Furthermore, Ca^{2+}-loaded S100B binds a peptide derived from the protein CapZ (the TRTK peptide) 5-fold more tightly when Zn^{2+} is present (*16*). Likewise, the Ca^{2+}-dependent binding of peptides derived from giant phosphoprotein, AHNAK, to S100B is enhanced by the presence of Zn^{2+} (*17*). Another S100 protein, S100A1, binds Zn^{2+} at nanomolar concentrations (*14*), and it activates myosin-associated protein kinase twitchin in a Ca^{2+}-dependent manner 1000-fold more efficiently when Zn^{2+} is bound. As with S100B, S100A1 has an increased affinity for its target proteins such as twitchin kinase (*18*) and synapsin IIa (*19*) in the presence of Zn^{2+}. Other S100 proteins that bind Zn^{2+} include S100A2 ($K_d = 4.6$ μM), S100A3 ($K_d = 1.5$ μM), S100A4 (affinity not reported), S100A5 ($[Zn^{2+}]_{0.5} = 2$ μM), S100A6 ($K_d = 0.1$ μM), and S100A7 ($K_d = 100$ μM) (*20*), and in each case a conformational change is observed upon Zn^{2+} binding. S100A9 was found to compete

† This work was supported by grants from the National Institutes of Health (GM58888 to D.J.W.) and from the American Cancer Society (RPG0004001-CCG to D.J.W.).

* Address correspondence to this author at the Department of Biochemistry and Molecular Biology. Phone: (410) 706-4354. Fax: (410) 706-0458. E-mail: dweber@umaryland.edu.

‡ Molecular and Cell Biology Program, University of Maryland School of Medicine.

§ Department of Biochemistry and Molecular Biology, University of Maryland School of Medicine.

[1] Abbreviations: ITC, isothermal titration calorimetry; NMR, nuclear magnetic resonance; TRTK, CapZ peptide (TRTKIDWNKILS); GFAP, glial fibrillary acidic protein; PKC, protein kinase C; GAP-43, growth-associated protein 43; MARCKS, myristoylated alanine-rich protein kinase C substrate; $p53^{367-388}$, p53 peptide (SHLKSKKGQSTSRHKKLMFKTE); $p53^{F385W}$, fluorescent p53 peptide (SHLKSKKGQSTSRHKKLMWKTE); DTT, dithiothreitol; TES, 2-[[2-hydroxy-1,1-bis(hydroxymethyl)ethyl]amino]ethanesulfonic acid; TPPI, time-proportional phase incrementation; TSP, 3-(trimethylsilyl)propionic acid-d_4 sodium salt; HSQC, heteronuclear single-quantum coherence; NOESY, nuclear Overhauser effect spectroscopy; HOHAHA, homonuclear Hartman−Hahn spectroscopy; HMQC, heteronuclear multiple-quantum coherence; DIPSI-2, decoupling in the presence of scalar interaction version 2; EDTA, ethylenediaminetetraacetic acid; BMRB, BioMagResBank; RMSD, root mean square difference; PDB, Protein Data Bank; WT, wild type; 3D, three dimensional.

10.1021/bi035334q CCC: $25.00
Published on Web 10/30/2003

with S100B for Zn^{2+} in gel-binding assays (*21*), and Zn^{2+} binding to the S100A8/A9 heterodimer modulates its binding to arachidonic acid (*22*) and its antimicrobial activity (*23*). S100A12 binds Zn^{2+} with relatively high affinity compared to other S100 proteins, and Zn^{2+} binding causes a large increase (~1500-fold) in its affinity for Ca^{2+} (*24*).

Mutational and spectroscopic studies were done in an attempt to elucidate the Zn^{2+} ligands in S100A2 and S100A3 (*25*, *26*), but only the Zn^{2+}-binding sites in S100A7 have been characterized at atomic resolution by X-ray crystallography (*27*). The crystal structure of Zn^{2+}-loaded S100A7 was solved, showing two identical Zn^{2+} sites per dimer at the dimer interface with coordinating residues from helix 1 (H17) and the pseudo-EF-hand (A24) of one subunit and two residues in the carboxyl tail of the other subunit (H86 and H90) (*27*). The Zn^{2+} ion is bound in trigonal-bipyramidal geometry with two side chain oxygen atoms of Asp-24 forming a bidentate ligand and the three histidine side chain nitrogen atoms liganded per Zn^{2+} ion. In S100A7, Zn^{2+} binding causes a slight increase in the distance between the two typical EF-hands, from 27.8 to 28.7 Å, whereas the pseudo-EF-hand was reoriented in a manner that more resembles a typical EF-hand in the presence of Zn^{2+}. The pseudo-EF-hand in S100A7 does not bind Ca^{2+} in the presence or absence of Zn^{2+} since it lacks three residues that are critical for binding Ca^{2+}. The potential target protein-binding cleft in S100A7 contracts somewhat in the Zn^{2+}-bound state with additional changes in the hydrophobic core of the protein. Unlike S100B, however, there is no evidence that Zn^{2+}-bound S100A7 has a changed affinity for Ca^{2+} or target proteins.

The three-dimensional structure of S100B is determined in the apo, Ca^{2+}-bound, and target peptide-bound states (*28*−*31*), but no structure is yet solved for S100B in the presence of Zn^{2+}. Characterizing the binding of Zn^{2+} is important because it induces a conformational change in S100B that is distinct from the conformational change induced by Ca^{2+} (*32*). Specifically, the distance between the two Ca^{2+}-binding sites within a subunit is closer (from 15 to 13 Å) in the presence of Zn^{2+} as detected by fluorescence resonance energy transfer measurements (*32*). Furthermore, at high concentrations of Zn^{2+}, saturation of several additional low-affinity sites in S100B causes an additional conformational change, which antagonizes Ca^{2+} binding and favors aggregation and precipitation of S100B (*14*). While it is clear that Zn^{2+} binds S100B and causes changes in its structure and activity, the details of the changes at or nearby the Zn^{2+}-binding sites of S100B are unknown. Thus, the work presented in this study identifies the putative Zn^{2+} ligands in the protein and begins to characterize the molecular details of the two high-affinity Zn^{2+}-binding sites in dimeric S100B. Additionally, NMR was used to characterize more global changes in the secondary structure of the protein that occur upon the addition of Zn^{2+} and provides initial structural data that is required to determine a high-resolution structure of Zn^{2+}-Ca^{2+}-bound S100B.

MATERIALS AND METHODS

Materials. All chemicals and reagents were of ACS grade or higher and were purchased from Sigma-Aldrich unless otherwise indicated. All buffers were passed through Chelex-100 resin to remove trace metals. $^{15}NH_4Cl$ and ^{13}C-labeled glucose were purchased from Cambridge Isotope Laboratories (Woburn, MA).

Peptide titrations were performed using a peptide based on the C-terminus of human p53 residues 367−388, acetyl-SHLKSKKGQSTSRHKKLMFKTE-am ($p53^{367-388}$), a fluorescent analogue of this peptide with a F385W mutation, acetyl-SHLKSKKGQSTSRHKKLMWKTE-am ($p53^{F385W}$), and a peptide derived from the α-subunit of the CapZ actin-binding protein, acetyl-TRTKIDWNKILS-am (TRTK peptide) (Biopolymer Laboratory, University of Maryland, Baltimore, MD). The peptides were all produced using solid-state peptide synthesis with the N- and C-termini acetylated (acetyl-) and amidated (-am), respectively. The purity (>99%) of the stock peptides was determined by HPLC, and their concentration and composition were checked by amino acid analysis (Analytical Biotechnology Services, Cambridge, MA).

Preparation of Wild-Type and Mutant S100B. A pET11b (Novagen, Inc., Madison, WI) expression vector containing the rat S100B gene (*33*) was used as the template for production of the S100B mutants using the QuickChange site-directed mutagenesis kit (Stratagene, La Jolla, CA) according to manufacturer's instructions. Mutations were confirmed by DNA sequencing (Biopolymer Laboratory, University of Maryland, Baltimore, MD). Clones were then transformed into HMS174(DE3) (Novagen) cells and selected for maximum expression of protein as detected by SDS−PAGE electrophoresis. Unlabeled, ^{15}N-labeled, and ^{13}C,^{15}N-labeled S100B were prepared and purified (>99%) under reducing conditions using procedures similar to those described previously (*28*, *33*) except DTT was used as a reducing agent instead of β-mercaptoethanol. The concentrations of wild-type and mutant S100B stock solutions were determined using the Bio-Rad protein assay (Bio-Rad) using wild-type S100B of known concentration as the standard. The concentration of this S100B standard was determined by amino acid analysis (Commonwealth Biotechnologies, Inc., Richmond, VA). The concentrated purified protein was stored at a concentration of 1−7 mM in 2 mM TES, pH 7.2, with 0.5 mM DTT at −80 °C until use. While S100B was purified and stored long term in DTT-containing buffer, it is necessary to remove the DTT for the isothermal titration calorimetry (ITC) experiments to eliminate ITC artifacts. However, the removal of DTT has no effect on the ability of S100B to bind calcium or target protein, nor does it affect the aggregation state of the protein; for consistency, DTT was removed for all of the experiments reported in this paper.

Fluorescence Spectroscopy. The Ca^{2+}-dependent interactions of the $p53^{F385W}$ peptide with wild-type S100B and mutants of S100B were performed using previously described fluorescence spectroscopy techniques (*13*). All fluorescence spectra were collected on an SLM-Aminco series 2 fluorescence spectrophotometer with the temperature maintained at 37 °C. The measurements were carried out in a quartz cuvette with a 0.2 and 1 cm excitation and emission path length, respectively. The excitation was set at 295 nm with a 4 nm slit width. The increase in emission at 338 nm was monitored during the addition of S100B to the solution containing peptide alone (*13*). All samples contained 14 μM $p53^{F385W}$, 10 mM $CaCl_2$, 10 mM TES, pH 7.2, and 15 mM NaCl, with the titrant containing the same buffer plus 150

Table 1: Parameters for NMR Experiments[a]

		parameters[b]			
experiment	dim	nucl	time pts	freq pts	acq time (ms)
2D ^{1}H,^{15}N fast HSQC	t_1	^{15}N	200	400	109.6
	t_2	^{1}H	512	1024	61.0
2D ^{1}H,^{15}N long-range HSQC	t_1	^{15}N[k]	100	512	11.0
	t_2	^{1}H	512	1024	61.0
3D ^{15}N-edited NOESY-HSQC[c]	t_1	^{1}H	80	256	11.1
	t_2	^{15}N	32	64	17.5
	t_3	^{1}H	512	1024	71.3
3D ^{15}N-edited HOHAHA-HSQC[d]	t_1	^{1}H	64	256	8.9
	t_2	^{15}N	32	64	17.5
	t_3	^{1}H	512	1024	71.3
3D ^{15}N,^{15}N-edited HMQC-NOESY-HSQC[c]	t_1	^{1}H	24	64	13.2
	t_2	^{15}N	24	64	13.2
	t_3	^{1}H	512	1024	71.3
3D HNHA	t_1	^{1}H	96	512	11.4
	t_2	^{15}N	30	128	15.4
	t_3	^{1}H	512	1024	61.0
3D CBCA(CO)NH	t_1	^{13}C[f]	55	256	6.1
	t_2	^{15}N	29	128	15.9
	t_3	^{1}H	512	1024	61.0
3D HNCACB[l]	t_1	^{15}N	29	256	15.9
	t_2	^{13}C[g]	56	128	6.2
	t_3	^{1}H	512	1024	61.0
3D HNCA	t_1	^{13}C[h]	56	112	18.6
	t_2	^{15}N	38	152	20.8
	t_3	^{1}H	512	1024	71.3
3D HNCO	t_1	^{13}C[i]	50	112	16.6
	t_2	^{15}N	32	152	17.5
	t_3	^{1}H	512	1024	71.3
4D ^{13}C,^{15}N-edited NOESY-HSQC[e]	t_1	^{13}C[j]	20	64	5.5
	t_2	^{1}H	64	128	7.6
	t_3	^{15}N	16	64	8.8
	t_4	^{1}H	256	512	36.6

[a] Data were collected in H_2O at 37 °C at 600.13 MHz for ^{1}H. [b] The number of points in the time domain is complex. The number of points in the frequency domain is real. The carrier frequencies were 4.658 and 120.0 ppm for ^{1}H and ^{15}N, respectively, unless otherwise noted. [c] The NOE mixing time was 150 ms. [d] The HOHAHA spin-lock time was 68 ms using a 10 kHz rf field strength and relaxation-compensated DIPSI-2 mixing sequence. [e] The NOE mixing time was 120 ms. [f] The ^{13}C carrier position was 46.0 ppm. [g] The ^{13}C carrier position was 45.226 ppm. [h] The ^{13}C carrier position was 56.00 ppm. [i] The ^{13}C′ carrier position was 173.77 ppm. [j] The ^{13}C carrier position was 42.99 ppm. [k] The ^{15}N carrier position was 200.00 ppm. [l] This experiment was optimized for collecting the $^{13}C_\beta$, and the HNCA experiment was used to assign $^{13}C_\alpha$.

μM wild-type or mutant S100B. The binding data fit a single-site binding model using Origin software (OriginLab Corp., Northampton, MA) with one peptide bound per S100B subunit using a hyperbolic curve fit.

NMR Spectroscopy. The NMR experiments performed for the sequence-specific resonance assignment of Zn^{2+}-Ca^{2+}-S100B are listed in Table 1. Heteronuclear NMR spectra were collected at 37 °C with a Bruker DMX600 NMR spectrometer (600.13 MHz for protons) equipped with four frequency channels and a triple-resonance three-axis gradient probe. Unless otherwise stated, a 1 s relaxation delay was used, and quadrature detection in the indirect dimensions was obtained with States−TPPI phase cycling (*34*). For most experiments, initial delays in the indirect dimensions were set to give zero- and first-order phase corrections of 90° and −180°, respectively (*35*). Data were processed using the processing program nmrPipe (*36*). Time−domain data in the indirect dimensions were extended by no more than one-third using standard linear prediction routines (*37*), except for data in constant time domains that were extended 2-fold using mirror-image linear prediction (*38*). All proton chemical shifts are reported with respect to the H_2O or HDO signal taken to be 4.658 ppm relative to external TSP (0.0 ppm) at 37 °C. The ^{13}C and ^{15}N chemical shifts were indirectly referenced using the following ratios of the zero-point frequencies at 37 °C: 0.10132905 for ^{15}N−^{1}H and 0.25144953 for ^{13}C−^{1}H (*39*−*41*).

Uniformly ^{15}N-labeled S100B was used to collect the 2D ^{1}H,^{15}N fast HSQC (*42*), 2D ^{1}H,^{15}N long-range HSQC (*43*), 3D ^{15}N-edited NOESY-HSQC, 3D ^{15}N-edited HOHAHA-HSQC (*34*, *42*), 3D ^{15}N,^{15}N-edited HMQC-NOESY-HSQC (*44*), and 3D HNHA (*45*). The ^{13}C,^{15}N-labeled S100B was used to collect 3D CBCA(CO)NH (*46*), 3D HNCACB (*47*), 3D HNCA (*48*), 3D HNCO (*48*), and 4D ^{13}C,^{15}N-edited NOESY-HSQC (*49*). For the HNCACB experiment, a longer delay (7.2 ms) was used to transfer magnetization solely to C_β prior to carbon data acquisition rather than the shorter delay (3.6 ms) that is more typically used for collection of both C_α and C_β data, as previously described (*47*). The fast HSQC detection scheme was incorporated in most of the pulse sequences, and pulse field gradients were used as needed to purge undesired magnetization (*50*).

Unless specified otherwise, NMR samples contained 3 mM ^{15}N- or ^{13}C,^{15}N-labeled S100B subunit, 3 mM zinc acetate, 10 mM $CaCl_2$, 0.34 mM NaN_3, 15 mM NaCl, 10 mM TES, pH 7.2, and 10% D_2O. Samples prepared in this manner were stable for more than 2 weeks. The optimal Zn^{2+} concentration was determined in titrations of Ca^{2+}-S100B with Zn^{2+} while monitoring the sample visually and with the 2D ^{1}H,^{15}N fast HSQC experiment. Significant protein aggregation and broadening of the 2D ^{1}H,^{15}N fast HSQC correlations were observed when the concentration of Zn^{2+} exceeded 1 equivalent of S100B subunit. The 1:1 S100B subunit:Zn^{2+} stoichiometry for the high-affinity Zn^{2+} site was confirmed by ITC analysis (see below). Titrations of the $p53^{367-388}$ or the TRTK peptide into Zn^{2+}-Ca^{2+}-S100B were performed, and chemical shift perturbations in the backbone ^{15}N and amide ^{1}HN correlations were determined.

Isothermal Titration Calorimetry. Binding of Zn^{2+} to wild-type and mutant S100B was analyzed by measuring heat changes during the titration of zinc acetate into the protein solution using a VP-ITC titration microcalorimeter (MicroCal, Inc., Northhampton, MA). All protein and metal ligand solutions were degassed under vacuum and equilibrated at 37 °C prior to titration. The sample cell (1.4 mL) contained 10 mM TES, pH 7.2, 15 mM NaCl, and 10 mM $CaCl_2$, with either 0.2 mM wild-type S100B, mutant S100B, or no protein, while the reference cell contained water. Upon equilibration, a 1.5 mM zinc acetate solution prepared in the same buffer as used in the sample cell was injected in 4 × 40 μL aliquots followed by 43 × 5 μL aliquots using the default injection rate with a 300 s interval between each injection to allow the sample to return to baseline. The resulting titration curves were corrected for the protein-free buffer control and analyzed using the Origin for ITC software supplied by MicroCal (Northampton, MA). Care was taken to properly clean the ITC sample cell and syringe prior to each titration. This was done by adding 5% Contrad detergent solution (Decon Laboratories, Inc., Bryn Mawr, PA), heating to 55 °C for 1 h, and then flushing the cell five times with ~2 mL of a 55 °C 5% Contrad detergent solution. After the detergent wash, the cell was rinsed three times with deionized H_2O, incubated with 0.5 M EDTA for 5 min, and then

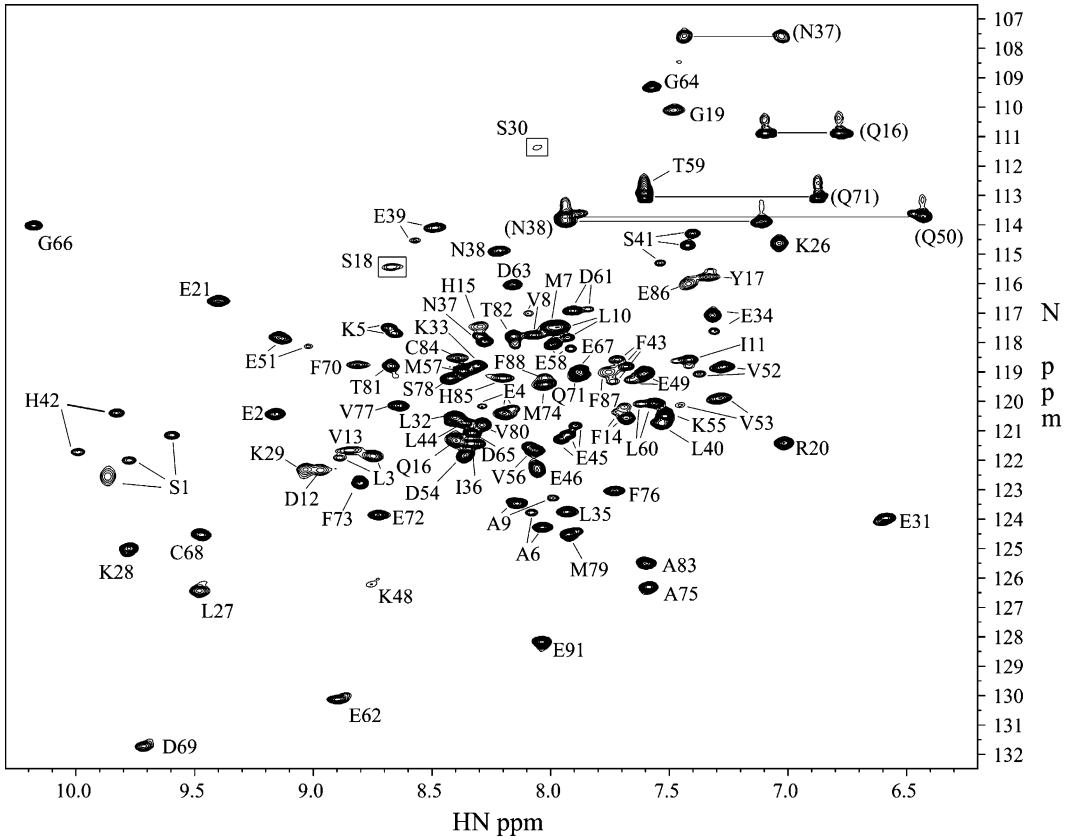

FIGURE 1: 2D ^1H,^{15}N fast HSQC of Zn^{2+}-Ca^{2+}-bound S100B shown together with the resonance assignments. The contours connected by the horizontal lines correspond to the glutamine and asparagine side chain NH_2 groups. Expression of recombinant S100B in *E. coli* yields three forms due to different N-terminal processing that include an N-terminal serine, methionine, or *N*-formylmethionine (*62*). This causes several residues (including S1, L3, E4, K5, A6, S41, H42, F43, L44, and E45) to exhibit multiple correlation peaks. The sample conditions were 3 mM ^{15}N-labeled S100B, 3 mM zinc acetate, 10 mM $CaCl_2$, 15 mM NaCl, 0.34 mM NaN_3, and 10 mM TES, pH 7.2, at 37 °C.

flushed with >300 mL of metal-free deionized H_2O before loading the next sample. The loading syringe was washed with >2 mL of 5% Contrad detergent solution and rinsed with >6 mL of deionized H_2O, 2 mL of 0.5 M EDTA, and finally >10 mL of metal-free deionized H_2O prior to use.

Molecular Model. The three-dimensional structures of Ca^{2+}-S100B (*29*) and TRTK-Ca^{2+}-S100B (*31*) were used as starting points for calculating models of Zn^{2+}-Ca^{2+}-S100B. The identity of the Zn^{2+} ligands was determined by ITC and mutational analyses, and the Zn^{2+} distance constraints used for the modeling, 2.18 Å for His$-N^{\epsilon 2}$ or $-N^{\delta 1}$ and 2.1 Å for Cys$-S^{\gamma}$ to Zn^{2+}, were based on the average distances determined from the crystal structures of Zn^{2+}-binding proteins as described by Christianson (*51*). Data from the 2D ^1H,^{15}N long-range HSQC experiments were used to determine the tautomerization state of the histidine residues except for His-85, which was not observable in the metal-bound state. Both H85$-N^{\epsilon 2}$ and $-N^{\delta 1}$ were tested as ligands in separate calculations with $N^{\delta 1}$ as a ligand giving the lowest energy models. Two models (models 1 and 2) were calculated for Zn^{2+},Ca^{2+}-S100B using the NMR structure of Ca^{2+}-loaded S100B as the starting point. In the first model, no modifications were made to the NMR structure of Ca^{2+}-S100B prior to the calculations (model 1). In the second model (model 2), helix 4 of Ca^{2+}-S100B was extended to Phe-87 by adding dihedral angle constraints to the previously unstructured C-terminal tail residues (C85−F87). This was done to provide the same secondary structure as that observed here for Zn^{2+}-Ca^{2+}-S100B. Last, modeling Zn^{2+}-Ca^{2+}-S100B was done using the TRTK-Ca^{2+}-S100B structure as the starting point (model 3). Because the secondary structure of Zn^{2+}-Ca^{2+}-S100B was found to be identical to that of the TRTK-bound S100B structure, it was not necessary to add any additional constraints to the starting structure. However, the TRTK peptide and all the constraints to the TRTK peptide were removed prior to this calculation. In all three models of Zn^{2+}-Ca^{2+}-S100B, a standard protocol for simulated annealing and refinement was used to refine the model using X-PLOR version 3.851.

RESULTS AND DISCUSSION

NMR Studies of Zn^{2+}-Ca^{2+}-S100B. Changes in the 2D $^1H-^{15}N$ HSQC spectrum of Ca^{2+}-bound S100B were monitored upon the addition of Zn^{2+}. In this titration, several HSQC correlations disappeared and then reappeared in the slow exchange regime and were the most narrow at 1 equivalent of Zn^{2+} per S100B subunit. Further additions of Zn^{2+} resulted in severe line broadening in the spectrum and precipitation of S100B. Nonetheless, at 1 equivalent of Zn^{2+}, the $^1H-^{15}N$ correlations remained sharp and high quality for an extended period of time (Figure 1) with a majority of the resonances shifted significantly from that found for Ca^{2+}-loaded S100B (Figure 2A). While some correlations could be assigned tentatively in the HSQC spectrum of the 1:1 Ca^{2+}-S100B:Zn^{2+} complex, these and the remaining resonances were unambiguously assigned using a standard set of multidimensional heteronuclear NMR experiments (Table 1). The sequence-specific assignments were completed for

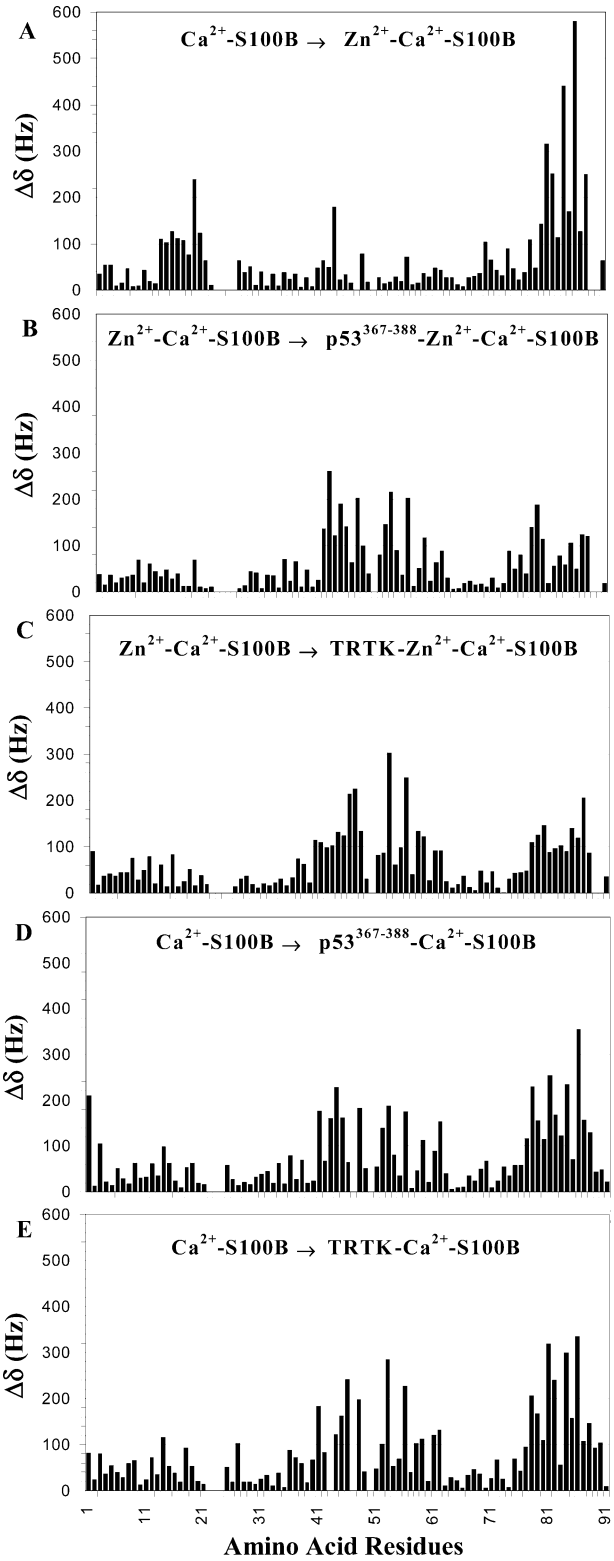

FIGURE 2: Combined ^1H and backbone ^{15}N chemical shift perturbations caused by the addition of (A) Zn^{2+} to Ca^{2+}-bound S100B, (B) $p53^{367-388}$ peptide to Zn^{2+}-Ca^{2+}-bound S100B, (C) TRTK peptide to Zn^{2+}-Ca^{2+}-bound S100B, (D) $p53^{367-388}$ peptide to Ca^{2+}-bound S100B (*13*, *30*) (BMRB accession number 4099), and (E) TRTK to Ca^{2+}-bound S100B (*31*) (BMRB accession number 5544).

all of the observable backbone resonances of Zn^{2+}-Ca^{2+}-bound S100B and most of the side chain resonances of this complex (BMRB accession number 5895).

The addition of Zn^{2+} to Ca^{2+}-bound S100B was found to significantly change the ^1H and ^{15}N chemical shift values (>100 Hz) for residues in helix 1 (D12−K16, S18, and G19), for a single residue in the hinge region (F43), and for residues in helix 4 and at the C-terminus (F70, S78, and T80−F88) of S100B (Figure 2A). When compared to Ca^{2+}-loaded S100B, the line width values for several of the backbone and/or side chain resonances of the Zn^{2+} complex broadened (C84, H85, F87, F88) or could no longer be detected (H25, E89, H90) due to exchange broadening effects that likely involve Zn^{2+} binding. Simultaneously, several other HSQC correlations (V80, T81, T82, T83) narrowed to some degree and increased in intensity upon the addition of Zn^{2+}, perhaps due to stabilization of an additional turn at the end of helix 4. These data are all consistent with the binding of Zn^{2+} to a region of S100B that includes helix 1 and the C-terminus of helix 4. Likewise, changes in chemical shift for residues in the typical EF-hand (i.e., Phe-70, >100 Hz) upon the addition of Zn^{2+} are consistent with a change in conformation in the typical EF-hand and may explain why Ca^{2+} ions bind more tightly to S100B in the presence of Zn^{2+} (*14*).

Solution Secondary Structure of Zn^{2+}-Ca^{2+}-S100B. NOE correlations, chemical shift index, amide−proton exchange rates, and scalar coupling constants ($^3J_{NH-H\alpha}$) were collected and analyzed for Zn^{2+}-Ca^{2+}-S100B in order to explore whether Zn^{2+} binding affects the secondary structure of Ca^{2+}-loaded S100B (Figure 3) (*41*, *52*−*54*). As expected, the secondary structure of Zn^{2+}-Ca^{2+}-S100B is very similar to that of apo, Ca^{2+}-loaded, and target peptide-bound S100B (Figure 4). As with the other states of S100B, Zn^{2+}-Ca^{2+}-S100B has four α-helices and two short *β*-strands that form a small antiparallel *β*-sheet consistent with two EF-hand helix−loop−helix Ca^{2+}-binding domains (Figure 3). The most significant difference in secondary structure is that the length of helix 4 is extended by four to five residues for Zn^{2+}-Ca^{2+}-S100B and target peptide-bound forms of S100B when compared to apo and Ca^{2+}-loaded S100B. Thus, the secondary structure of Zn^{2+}-Ca^{2+}-S100B is most similar to that of Ca^{2+}-S100B when it is bound to a target peptide.

Target Peptide Binding to Zn^{2+}-Ca^{2+}-S100B. Addition of target peptides such as TRTK and $p53^{367-388}$ to Zn^{2+}-Ca^{2+}-S100B caused similar changes in 2D $^1H-^{15}N$ HSQC correlations (Figure 2B,C) as found upon peptide addition to Ca^{2+}-S100B (Figure 2D,E). For example, additions of the $p53^{367-388}$ peptide perturbed resonances (>100 Hz) for residues in the hinge region (S41−E45, I47, K48), helix 3 (V52, V53, V56, T59), helix 4 (S78−V80), and the C-terminal loop (H85, F87, F88) of Zn^{2+}-Ca^{2+}-S100B (Figure 2B). Similarly, additions of the TRTK peptide perturbed resonances for residues in the hinge region (L40−K48), helix 3 (V53, V56, E58, T59), helix 4 (S78−V80, A83), and the C-terminal loop (H85−F87) of Zn^{2+}-Ca^{2+}-S100B (Figure 2C). However, the chemical shift changes occurring in helix 4 and the C-terminal loop are lesser in magnitude with peptide addition to Zn^{2+}-Ca^{2+}-S100B (Figure 2B,C) than with peptide addition to Ca^{2+}-S100B (Figure 2D,E). While the addition of target peptides to Ca^{2+}-S100B significantly changes the chemical shift values for several residues of S100B ($p53^{367-388}$, 11 residues change; TRTK-peptide, 10 residues change; >100 Hz), fewer changes are observed when target peptides are added to Zn^{2+}-Ca^{2+}-S100B ($p53^{367-388}$, 7 residues change; TRTK-peptide, 6 residues change; >100 Hz). These results may explain why target peptides bind the Zn^{2+} complex with higher affinity since

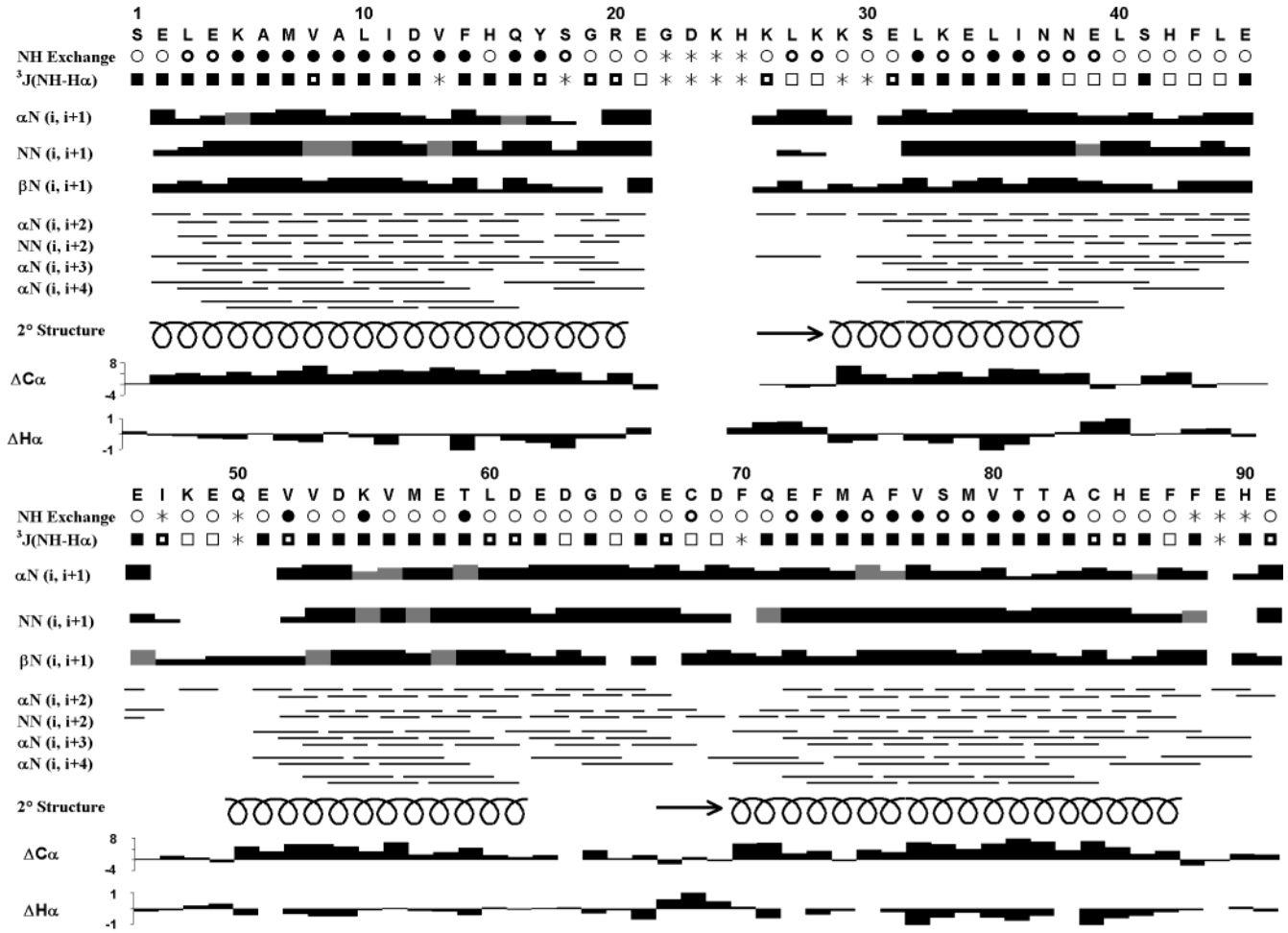

FIGURE 3: Diagram of NMR data used to determine the secondary structure of Zn^{2+}-Ca^{2+}-S100B. Amide proton exchange rates are classified as slow (T > 18 h), medium (0.25 h < T < 18 h), and fast (T < 0.25 h) with solid, half-filled, and empty circles, respectively. The $^3J_{NH-H\alpha}$ couplings are indicated as solid boxes for <6 Hz, half-filled boxes for between 6 and 8 Hz, and empty boxes for >8 Hz. Data for residues with asterisks were not available. The NOE strength is indicated by bar height (strong, medium, medium weak, weak, or very weak) with gray indicating ambiguous data due to overlapping peaks and horizontal lines connecting indicating the participating residues. Chemical shift deviations of $^{13}C_\alpha$ and $^1H_\alpha$ from the random coil values are given as positive values for upfield shifts and negative values for downfield shifts (*41*, *53*). The secondary structure is indicated as a coil for the α-helix and an arrow for the *β*-sheet.

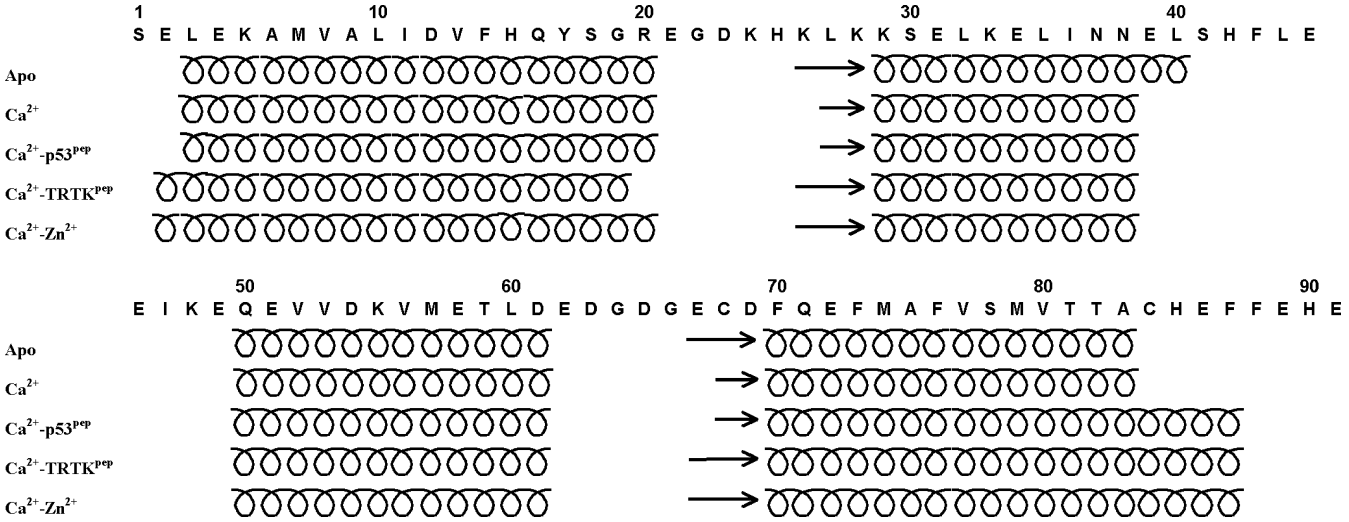

FIGURE 4: Comparison of the secondary structures of apo (*33*), Ca^{2+} (*29*), Ca^{2+}-$p53^{367-388}$ peptide (*55*), Ca^{2+}-TRTK peptide (*31*), and Zn^{2+}-Ca^{2+}-bound S100B. The secondary structure is indicated as a coil for the α-helix and an arrow for the *β*-sheet.

fewer/smaller conformational changes are required for target peptide binding to the C-terminus of Zn^{2+}-Ca^{2+}-S100B as compared to Ca^{2+}-bound S100B.

Further evidence that Zn^{2+} binding to Ca^{2+}-bound S100B induces a structural change at the C-terminus of S100B similar to that found for target peptide binding is provided

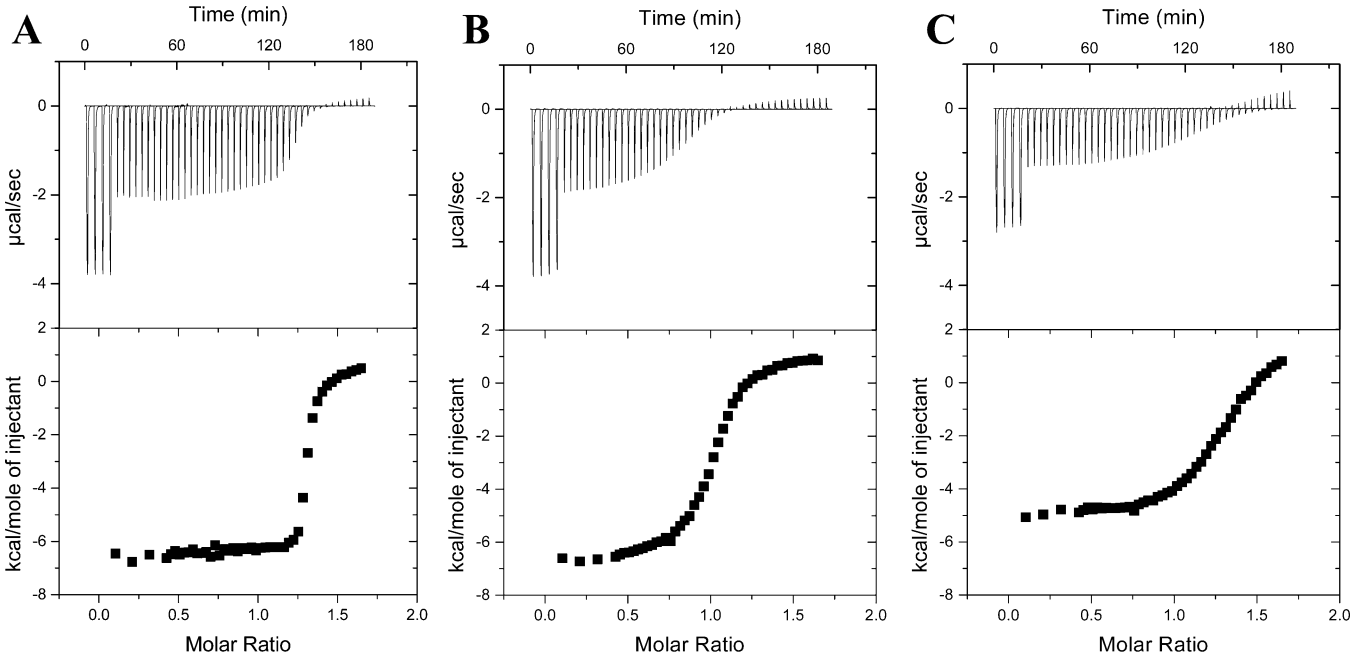

FIGURE 5: Typical isothermal titration calorimetry curves of Zn^{2+} binding to (A) wild-type, (B) H25A, and (C) H85A S100B showing their decreasing affinity for Zn^{2+} (WT > H25A > H85A). ITC analysis was used to generate the thermodynamic values for the interaction of Zn^{2+} with wild-type and mutated S100B as summarized in Table 2 and as described in the Materials and Methods section. Briefly, 1.5 mM Zn^{2+} was injected into Ca^{2+}-S100B while monitoring the heat released over time (shown in the top panels of A−C) with 40 μL injected for the first four points to expedite the experiment, while the remaining 43 points were 5 μL injections. The heat released per injection is then normalized per mole of Zn^{2+} injected and plotted against the molar ratio of Zn^{2+} to S100B monomer (shown in the bottom panels of A−C).

Table 2: Summary of $p53^{F385W}$ Peptide and Zn^{2+} Binding to WT and Mutant S100B

	$p53^{F385W}$ binding		Zn^{2+} binding				
S100B	K_d (μM)	fold Δ in K_d	K_d (nM)	fold Δ in K_d	ΔG (kcal/ mol)	ΔH (kcal/ mol)	ΔS (cal mol^{-1} deg^{-1})
H90A	9.4 ± 2.3	2.5	182.3 ± 6.2	1.9	−9.56 ± 0.02	−6.56 ± 0.07	9.7 ± 0.27
H85A	5.7 ± 1.0	1.5	1166.1 ± 78.6	12.4	−8.42 ± 0.02	−4.74 ± 0.06	11.9 ± 0.35
C84A	17.0 ± 2.2	4.5	>2654.0[a]	>28.2[a]	NA	NA	NA
C68A	18.9 ± 0.5	5.0	119.1 ± 12.6	1.3	−9.83 ± 0.06	−6.67 ± 0.13	10.2 ± 0.32
H42A	6.6 ± 0.8	1.7	130.3 ± 36.3	1.4	−9.81 ± 0.16	−5.80 ± 0.10	13.0 ± 0.47
H25A	8.0 ± 0.2	2.1	555.0 ± 86.9	5.9	−8.89 ± 0.09	−6.61 ± 0.14	7.3 ± 0.18
H15A	10.5 ± 3.5	2.8	2654.0 ± 883.3	28.2	−7.98 ± 0.21	−2.86 ± 0.44	16.5 ± 2.03
WT	3.8 ± 0.3	1.0	94.2 ± 16.7	1.0	−9.99 ± 0.10	−6.24 ± 0.17	12.1 ± 0.21

[a] Could not detect any Zn^{2+} binding to C84A so it is assumed to have a lower binding affinity than H15A.

by the observation that several HSQC correlations for the same residues (T81−F87) narrow during titrations with Zn^{2+}, $p53^{367-388}$, or the TRTK peptides (*13*, *55*). This line narrowing is likely due to the stabilization of the C-terminal end of helix 4. While binding target peptides to Ca^{2+}-S100B causes similar changes to helix 4 of Ca^{2+}-S100B as does Zn^{2+} binding, target peptide binding does not induce changes in helix 1 as found upon the addition of Zn^{2+}. Another difference is that target peptide binding causes chemical shift changes in the hinge region ($p53^{367-388}$ peptide, S41, F43−E45, K48; TRTK peptide, L40−K48) and helix 3 ($p53^{367-388}$ peptide, V52, V53, V56, T59, E62; TRTK peptide, V53, V56, E58, T59) during titrations (Figure 2), which are not observed upon Zn^{2+} binding. Thus, Zn^{2+} binding to Ca^{2+}-S100B does not completely mimic the chemical shift perturbations and structural effects of target peptide binding to Ca^{2+}-S100B.

ITC Analysis of Zn^{2+} Binding to Wild-Type and Mutant S100B. To identify ligands on S100B that bind Zn^{2+}, point mutations of all the histidine and cysteine residues were prepared, and changes in their Zn^{2+}-binding affinity were monitored using isothermal titration calorimetry (ITC). ITC measurement of wild-type S100B showed one high-affinity Zn^{2+}-binding site per S100B subunit with a disassociation constant (K_d = 94.2 ± 16.7 nM; Figure 5A) consistent with values determined previously by equilibrium dialysis (K_d ~ 100 nM) (*56*). Equilibrium dialysis of wild-type S100B also showed that two (or more) additional lower affinity (K_d = 2 μM) Zn^{2+} sites are present per S100B subunit (*14*). However, in this study, characterization of the low-affinity sites was not done for several reasons. First, these weaker Zn^{2+}-binding sites are not significantly occupied inside the cell because free Zn^{2+} concentrations only approach low nanomolar concentrations (*57*). Second, at greater than a 1 to 1 ratio of Zn^{2+} to S100B subunit, precipitation of S100B occurs, which makes it very difficult to obtain accurate measurement of these low-affinity sites using ITC. Last, while positive (endothermic) isotherms in the ITC data (Figure 5) appear for the weak binding sites (i.e., once the tight Zn^{2+} sites are occupied), none of the point mutations tested in this study eliminate this small positive (endothermic) contribution. Thus, the low-affinity Zn^{2+}-binding sites are both weak and

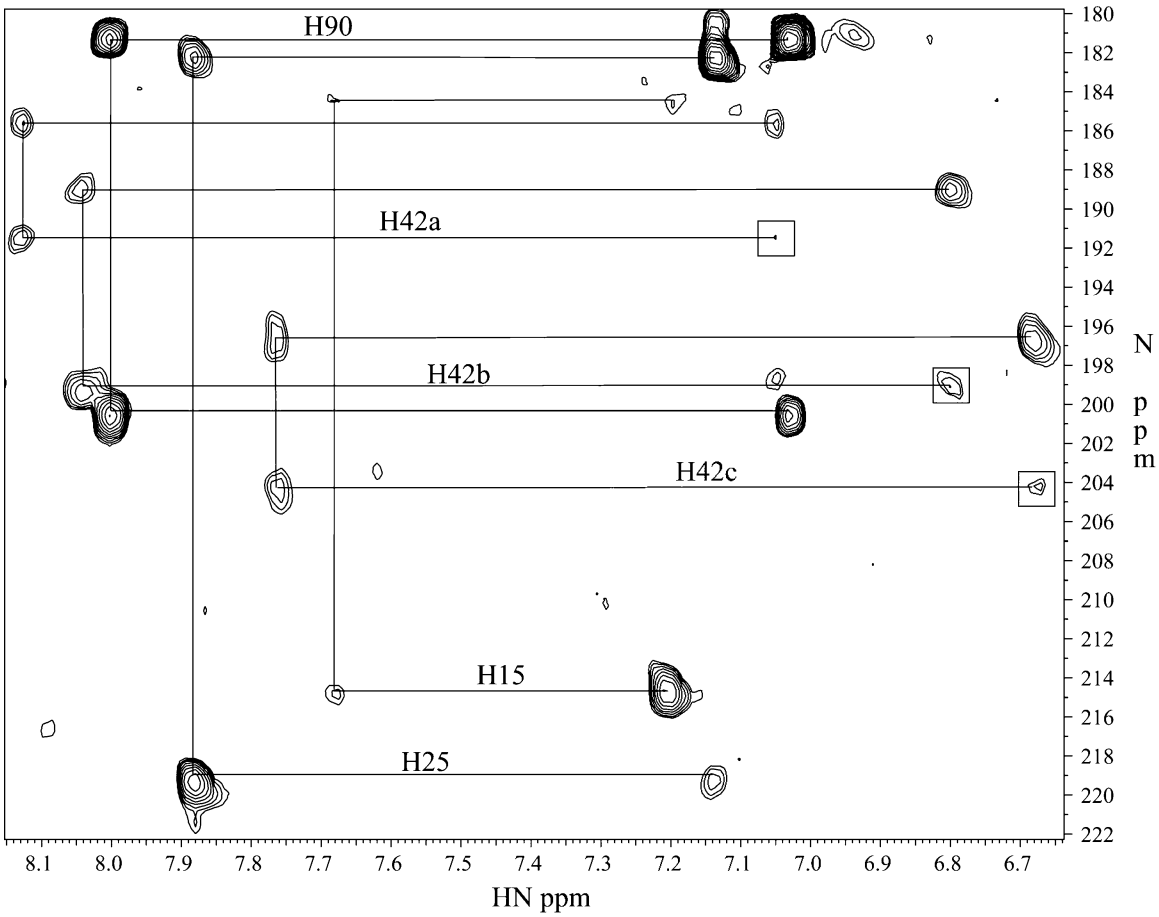

FIGURE 6: LR-HSQC of Ca^{2+}-S100B showing correlations for the histidine side chain ring protons and amides in Ca^{2+}-bound S100B. In this sample, the conformation of the rings favors the $N^{\epsilon 2}-H$ tautomer for His-25 (89%), His-42 (82%), and His-90 (85%), allowing $N^{\delta 1}$ to be available as a Zn^{2+} ligand, whereas His-15 favors the $N^{\delta 1}-H$ tautomer (81%), making $N^{\epsilon 1}$ available as a ligand.

independent from the high-affinity binding site as previously described (*14*). For these reasons, the high-affinity Zn^{2+} sites on S100B are the focus of this study. Nonetheless, the low-affinity sites may be important in extracellular activities of S100B where Zn^{2+} levels are higher. For instance, extracellular levels of S100B are high in Alzheimer's patients (*58*), and Zn^{2+}-induced precipitation of proteins, such as S100B, may contribute to Alzheimer's disease pathology since metal chelating antibiotics help patients clinically and specific Zn^{2+} chelators can partially dissolve protein plaques typical of Alzheimer's disease (*59*, *60*).

Comparisons of wild-type and mutant S100B binding data were made in order to identify residues involved in Zn^{2+} binding to the high-affinity binding site. Specifically, ITC data show that H42A and C68A mutant proteins do not significantly change S100B Zn^{2+}-binding affinity (Table 2), whereas the H90A, H25A, and H85A mutations cause a 1.9-, 5.9-, and 12.4-fold reduction in Zn^{2+} binding, respectively. Greater than a 28-fold loss in Zn^{2+}-binding activity (Table 2) was observed for the H15A and C84A mutants when compared to wild-type S100B, indicating that His-15 and Cys-84 provide the largest contributions toward binding Zn^{2+}. As a control, it was found that all of the S100B mutant proteins retained the ability to bind the $p53^{367-388}$ peptide in a Ca^{2+}-dependent manner, thus showing that the mutations did not disrupt the function of S100B (Table 2). Together, these data indicate that the high-affinity Zn^{2+} site in S100B includes His-15, His-25, Cys-84, His-85, and perhaps His-90 as Zn^{2+} ligands. Importantly, the locations of His-15, His-25, Cys-84, and His-85 agree with chemical shift changes observed upon Zn^{2+} binding (Figure 2) and are in locations analogous to the ligands found in the S100A7 Zn^{2+} site determined previously by X-ray crystallography (*27*).

The Zn^{2+}-Binding Site in Zn^{2+}-Ca^{2+}-S100B. Comparison of wild-type S100B and the five histidine mutants of S100B (H15A, H25A, H42A, H85A, and H90A) in long-range HSQC (LR-HSQC) experiments was done to assign the side chain resonance of the histidine residues in S100B. In Ca^{2+}-bound S100B, the tautomerization state of the histidine side chain rings was found to favor the $N^{\epsilon 2}-H$ tautomer for His-25 (89%), His-42 (82%), and His-90 (85%), whereas His-15 favors the $N^{\delta 1}-H$ tautomer (81%) as determined from characteristic $^{1}H-^{15}N$ correlations in the LR-HSQC (Figure 6). The LR-HSQC correlations for the side chain ring residues of His-85 were not observed in Ca^{2+}-bound S100B or Zn^{2+}-Ca^{2+}-S100B. It was also found that the stepwise addition of Zn^{2+} eliminates the minor tautomerization component for each observable histidine side chain such that the histidine rings are completely (100%) in the tautomerization state originally favored in the Ca^{2+}-bound S100B. The addition of Zn^{2+} almost immediately broadens the $N^{\delta 1}-H^{\epsilon 1}$ side chain correlation for His-15 with the $N^{\epsilon 2}-H^{\epsilon 1}$ and $N^{\epsilon 2}-H^{\delta 2}$ correlations showing significant broadening later in the titration. At the end of the titration (1 equivalent of Zn^{2+} bound), only the correlations for $N^{\epsilon 2}-H^{\delta 2}$ of His-25 and His-90 and, while broadened to some degree, all of

the His-42 correlations were observable. Furthermore, the histidine residues of S100B that most affect Zn^{2+} binding as determined by mutagenesis and ITC analysis are locked into one tautomer earlier in the titration (H15 > H25 > H90) and are broadened more quickly (H85 > H15 > H25 > H90 > H42) than the side chain histidine residues that had lesser effects on Zn^{2+} binding as determined by ITC. While the mechanism for exchange broadening is not completely clear, it may be that Zn^{2+} binding initiates motion for a ligand [and/or for residue(s) nearby] that occurs in the intermediate exchange regime. Nonetheless, data from NMR and ITC data of wild-type S100B and mutants of S100B indicate that C84−S^{γ}, $N^{\epsilon 2}$ of His-15, $N^{\delta 1}$ of His-25 and His-90 coordinate Zn^{2+} with an additional ligand coming from one of the two possible tautomers of His-85.

At this point, it was possible to calculate a reasonable model for Zn^{2+}-Ca^{2+}-S100B using the three-dimensional structures of the Ca^{2+}-S100B (*29*) and TRTK-Ca^{2+}-S100B (*31*) as starting points. Three models of Zn^{2+}-Ca^{2+}-S100B were calculated starting with either Ca^{2+}-bound S100B (models 1 and 2) or peptide−Ca^{2+}-bound S100B (model 3). In initial calculations, both H85−$N^{\epsilon 2}$ and −$N^{\delta 1}$ were tested as ligands in separate calculations, and in all cases, the use of $N^{\delta 1}$ as the His-85 ligand provided the lowest energy models. In the final calculations, all three models were of low energy and showed reasonable Zn^{2+} coordination geometry using the five ligands selected as input (H15−$N^{\epsilon 2}$, H25−$N^{\delta 1}$, C84−S^{γ}, H85−$N^{\delta 1}$, and H90−$N^{\delta 1}$). The known secondary structure of Zn^{2+}-Ca^{2+}-S100B (Figure 3) was satisfied for models 2 and 3, but in model 1, the Zn^{2+} constraints alone were not sufficient to induce the additional turn of helix 4 observed by NMR spectroscopy (Zn^{2+}-Ca^{2+}-S100B vs Ca^{2+}-S100B; Figure 4). Models 2 and 3 were very much alike (backbone RMSD = 2.24 Å) and similar to that of the trigonal-bipyramidal-type coordinating geometry found in the Zn^{2+} site of S100A7 (*27*) (Figure 7C). However, it is important to state that the atomic level details for these structural models for Zn^{2+}-Ca^{2+}-S100B require confirmation using more rigorous high-resolution NMR and/or X-ray crystallographic methodologies.[2]

CONCLUSIONS

In this study, the Zn^{2+}-binding site on Ca^{2+}-bound S100B was examined using NMR spectroscopy and site-directed mutagenesis. Specifically, His-15, His-25, Cys-84, His-85, and perhaps His-90 of S100B are involved in coordinating Zn^{2+} in a site that is very similar to that observed in the X-ray crystal structure of S100A7.[3] For S100B, titrations of Zn^{2+} perturb chemical shift values and/or secondary structure in Ca^{2+}-bound S100B that are potentially providing insights about how the binding of Zn^{2+} enhances calcium- and target protein-binding affinities.

The finding that S100B uses the side chain moieties of C84 and H85 as ligands with no intervening residues is a bit surprising since there are no known Cys-His Zn^{2+}-binding motifs such as this currently in the literature. However, the lack of intervening residues between Zn^{2+} ligands is not unprecedented since there are several such examples including a structural Zn^{2+} site in the RNA polymerase subunit RPB10 (Cys-Cys), cocatalytic Zn^{2+} sites in *Escherichia coli* alkaline phosphatase (His-Asp), human glyoxalase II (Asp-His), and *Stenotrophomonas maltophilia* β-lactamase (Asp-His), and protein interface Zn^{2+} sites (Glu-Glu) in human interferon-$\alpha_{2\beta}$ dimer (Glu-Glu), human prolactin receptor/growth hormone (Asp-His), and the Shaw T1 tetramer (Cys-Cys) (*61*) to name some. In the S100 protein family, the Cys-His motif is conserved in 5 out of 17 (29.4%) proteins (S100B, S100A3, S100A11, S100A14, and S100P), but only three of the five are known to bind Zn^{2+} (S100B, S100A3,

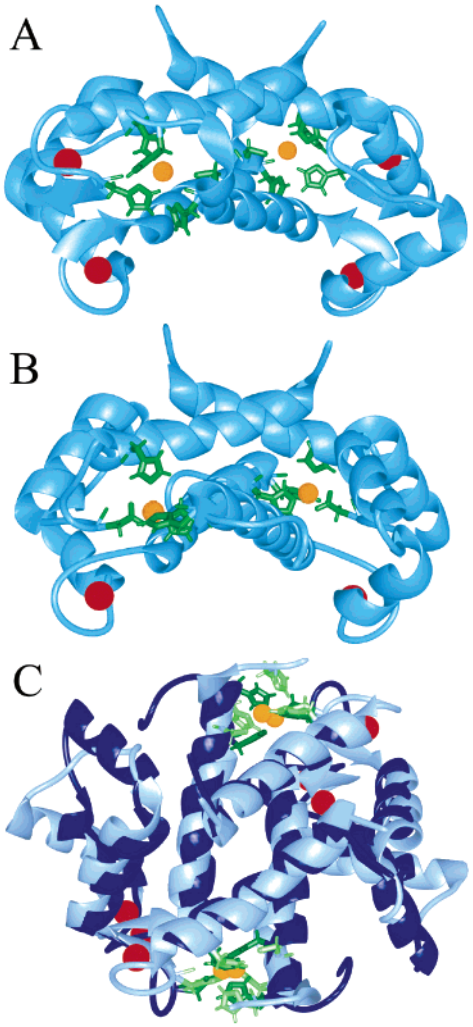

FIGURE 7: Location of the high-affinity Zn^{2+} site in S100A7 and S100B. (A) Zn^{2+}-Ca^{2+}-S100B (model 2) showing Zn^{2+} (orange spheres) and its ligands His-15, His-25, Cys-84, His-85, and His-90 (green) compared to (B) the X-ray crystal structure of Zn^{2+}-bound S100A7 showing Zn^{2+} and its ligands His-17, Asp-25, His-86, and His-90 (*27*) (PDB accession number 2PSR). (C) Overlay of Zn^{2+}-Ca^{2+}-S100B model 2 (light blue and green) and S100A7 (dark blue and green). Notice that the S100B dimer binds two Ca^{2+} ions (red) in its pseudo-EF-hands and two Ca^{2+} ions in its typical EF-hands, while S100A7 can only bind two Ca^{2+} in its typical EF-hands. S100A7 contains an extra helix in the region analogous to the variable loop in S100B, but the regions involved in forming the Zn^{2+} site (helix 1 and helix 4) have very similar orientations, and the Zn^{2+} site itself is similarly located when the two complexes are compared.

[2] A high-resolution solution NMR structure determination of Zn^{2+}-Ca^{2+}-S100B is underway and will be reported elsewhere.

[3] While it appears that His-90 of S100B is a weak ligand, it does seem to be involved in coordinating Zn^{2+}. This is supported by data from the H90A mutant, which caused a significant but small decrease in Zn^{2+} affinity (~2-fold). Another possibility from modeling is that the H90A mutation may be compensated by the availability of other potential ligands from S100B (E89 or E91) that could replace the mutated His-90.

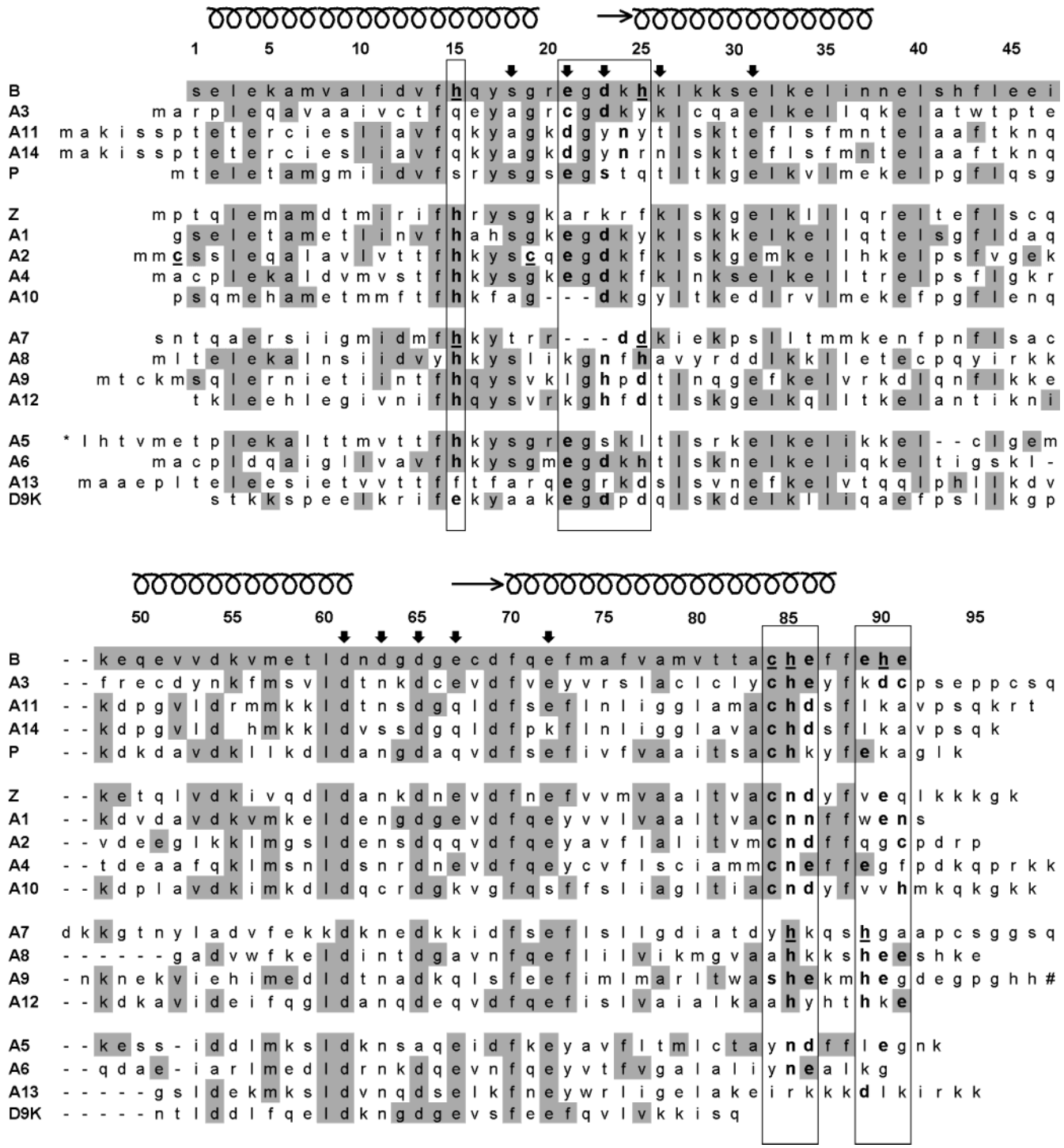

FIGURE 8: Alignment of the amino acid sequences of the S100 protein family members illustrating a proposed Zn^{2+}-binding motif common to several S100 proteins. The boxed regions contain conserved regions of amino acid residues that are capable of supplying ligands that can coordinate Zn^{2+}. Amino acids that are known to coordinate Zn^{2+} in other proteins are shown in bold with the most commonly utilized ones being His, Cys, Asp, and Glu, while Asn and Ser were used less often (*61*). Residues known to coordinate Zn^{2+} in S100B, S100A2 (*26*), and S100A7 (*27*) are underlined. All S100 family protein sequences given are of human and are aligned to and numbered according to the sequence of human S100B. While rat S100B was used in this study, it is 97.8% homologous with human S100B with differences in only two residues; human Asn-62 and Ala-78 are Glu-62 and Ser-78 in rat. The secondary structure of Zn^{2+}-Ca^{2+}-S100B is indicated by the coil and arrows at the top of the alignment for the α-helix and *β*-sheet, respectively. Downward arrows show the locations of the Ca^{2+} ligands in the conserved N-terminal pseudo-EF-hand and in the C-terminal typical EF-hand. The amino acid sequences of S100A5 and S100A9 were truncated to accommodate the figure; the missing sequence for the N-terminus of S100A5 (*) is mpaawilwahshse, and the missing sequence for the C-terminus of S100A9 (#) is hkpglgegtp.

and S100P), and of these three, S100P binds very weakly (K_d = ~1 mM). Since Asn has been shown to be a ligand for Zn^{2+} (*61*), the five other S100 proteins (S100A1, S100A2, S100A4, S100A10, and S100Z) that have Cys-Asn in the C-terminal loop could possibly coordinate Zn^{2+} in a manner similar to that of the Cys-His sequence, and of these three are known to bind Zn^{2+} (S100A1, S100A2, and S100A4). Therefore, 10 of 17 S100 proteins have either the Cys-His or Cys-Asn sequence in its C-terminus, which could potentially be involved in binding Zn^{2+}.

On the basis of homologies to S100B and S100A7, it is predicted that S100A1, S100A2, S100A4, S100A8, S100A9, S100A10, and S100A12 bind Zn^{2+} in a location similar to the sites found in S100B and S100A7. Ligands comprising the high-affinity Zn^{2+}-binding site in S100B are from the C-terminus and helix 1, and it is likely that several S100 proteins bind Zn^{2+} with similarly positioned residues (Figure 8). For example, in helix 1, the critically important Zn^{2+} ligand of S100B, His-15 (Table 2), is conserved in 12 out of the 17 (70.6%) S100 protein family members. Furthermore, all 17 S100 protein family members have a Cys, His, Asp, or Glu residue between Glu-21 and His-25 (using S100B numbering) including S100B, which has His-25, and S100A7, which has Asp-24 as liganding residues. In the C-terminus of S100 proteins (C84−E91; S100B numbering), 16 out of the 17 (94.1%) S100 proteins have one or more Cys, His, Asp, or Glu residue(s) in this region including S100B, which has Cys-84, a critically important residue for binding Zn^{2+} (Table 2). While a similar binding location for Zn^{2+} is found in S100B and S100A7 (*27*), there is some divergence in the exact location of residues used as Zn^{2+} ligands among these two S100 family members. In addition, the Zn^{2+}-binding ligands diverge a bit further in sequence comparisons to some other S100 proteins. For example, mutation of Cys-3 in S100A2 significantly decreases the Zn^{2+} affinity of this S100 protein (*26*), and spectroscopic evidence shows S100A3 uses multiple cysteine residues in regions of the protein that are not analogous to the sites in S100B and S100A7 (*25*). Furthermore, several other S100 proteins have additional cysteine residues, some of which are equivalent to Cys-3 of S100A2, and other S100 proteins have multiple possibilities for metal liganding residues in their variable C-terminal tails (Figure 8). Thus, it will be necessary to characterize the Zn^{2+}-binding sites for several S100 proteins before any definitive conclusions can be made about whether a common Zn^{2+}-binding site occurs in the S100 protein family.

ACKNOWLEDGMENT

This study made use of the NMR facility at the University of Maryland, Baltimore (UMB). The 600 MHz NMR spectrometer in the UMB NMR facility was purchased with funds from the University of Maryland and the NIH shared instrumentation grant program (S10RR10441-01 to D.J.W.). Microcalorimetry experiments were performed in the University of Maryland School of Medicine Microcalorimetry Laboratory, which is supported by the School of Medicine's Research Equipment Enhancement Fund.

REFERENCES

1. Donato, R. (2001) *Int. J. Biochem. Cell Biol. 33*, 637−668.
2. Berridge, M. J., Bootman, M. D., and Roderick, H. L. (2003) *Nat. Rev. Mol. Cell. Biol. 4*, 517−529.
3. Weber, D. J., Rustandi, R. R., Carrier, F., and Zimmer, D. B. (2000) *Interaction of dimeric S100B(ββ) with the tumor suppressor protein: A model for Ca-dependent S100-target protein interactions*, Kluwer Academic Publishers, Dordrecht, The Netherlands.
4. Bianchi, R., Verzini, M., Garbuglia, M., Giambanco, I., and Donato, R. (1994) *Biochim. Biophys. Acta 1223*, 354−360.
5. Bianchi, R., Giambanco, I., and Donato, R. (1993) *J. Biol. Chem. 268*, 12669−12674.
6. Wilder, P. T., Rustandi, R. R., Drohat, A. C., and Weber, D. J. (1998) *Protein Sci. 7*, 794−8.
7. Baudier, J., Mochly-Rosen, D., Newton, A., Lee, S. H., Koshland, D. E., Jr., and Cole, R. D. (1987) *Biochemistry 26*, 2886−2893.
8. Lin, L. H., Van Eldik, L. J., Osheroff, N., and Norden, J. J. (1994) *Brain Res. Mol. Brain Res. 25*, 297−304.
9. Sheu, F. S., Huang, F. L., and Huang, K. P. (1995) *Arch. Biochem. Biophys. 316*, 335−342.
10. Delphin, C., Ronjat, M., Deloulme, J. C., Garin, G., Debussche, L., Higashimoto, Y., Sakaguchi, K., and Baudier, J. (1999) *J. Biol. Chem. 274*, 10539−10544.
11. Baudier, J., Delphin, C., Grunwald, D., Khochbin, S., and Lawrence, J. J. (1992) *Proc. Natl. Acad. Sci. U.S.A. 89*, 11627−11631.
12. Lin, J., Blake, M., Tang, C., Zimmer, D., Rustandi, R. R., Weber, D. J., and Carrier, F. (2001) *J. Biol. Chem. 276*, 35037−35041.
13. Rustandi, R. R., Drohat, A. C., Baldisseri, D. M., Wilder, P. T., and Weber, D. J. (1998) *Biochemistry 37*, 1951−1960.
14. Baudier, J., Glasser, N., and Gerard, D. (1986) *J. Biol. Chem. 261*, 8192−8203.
15. Baudier, J., and Gerard, D. (1986) *J. Biol. Chem. 261*, 8204−8212.
16. Barber, K. R., McClintock, K. A., Jamieson, G. A., Jr., Dimlich, R. V., and Shaw, G. S. (1999) *J. Biol. Chem. 274*, 1502−1508.
17. Gentil, B. J., Delphin, C., Mbele, G. O., Deloulme, J. C., Ferro, M., Garin, J., and Baudier, J. (2001) *J. Biol. Chem. 276*, 23253−23261.
18. Heierhorst, J., Mann, R. J., and Kemp, B. E. (1997) *Eur. J. Biochem. 249*, 127−133.
19. Heierhorst, J., Mitchelhill, K. I., Mann, R. J., Tiganis, T., Czernik, A. J., Greengard, P., and Kemp, B. E. (1999) *Biochem. J. 344* (Part 2), 577−583.
20. Franz, C., Durussel, I., Cox, J. A., Schafer, B. W., and Heizmann, C. W. (1998) *J. Biol. Chem. 273*, 18826−18834.
21. Raftery, M. J., Harrison, C. A., Alewood, P., Jones, A., and Geczy, C. L. (1996) *Biochem. J. 316* (Part 1), 285−293.
22. Kerkhoff, C., Vogl, T., Nacken, W., Sopalla, C., and Sorg, C. (1999) *FEBS Lett. 460*, 134−138.
23. Sohnle, P. G., Hunter, M. J., Hahn, B., and Chazin, W. J. (2000) *J. Infect. Dis. 182*, 1272−1275.
24. Dell'Angelica, E. C., Schleicher, C. H., and Santome, J. A. (1994) *J. Biol. Chem. 269*, 28929−28936.
25. Fritz, G., Heizmann, C. W., and Kroneck, P. M. (1998) *Biochim. Biophys. Acta 1448*, 264−276.
26. Stradal, T. B., Troxler, H., Heizmann, C. W., and Gimona, M. (2000) *J. Biol. Chem. 275*, 13219−13227.
27. Brodersen, D. E., Nyborg, J., and Kjeldgaard, M. (1999) *Biochemistry 38*, 1695−1704.
28. Drohat, A. C., Amburgey, J. C., Abildgaard, F., Starich, M. R., Baldisseri, D., and Weber, D. J. (1996) *Biochemistry 35*, 11577−11588.
29. Drohat, A. C., Baldisseri, D. M., Rustandi, R. R., and Weber, D. J. (1998) *Biochemistry 37*, 2729−2740.
30. Rustandi, R. R., Baldisseri, D. M., and Weber, D. J. (2000) *Nat. Struct. Biol. 7*, 570−574.
31. Inman, K. G., Yang, R., Rustandi, R. R., Miller, K. E., Baldisseri, D. M., and Weber, D. J. (2002) *J. Mol. Biol. 324*, 1003−1014.
32. Chaudhuri, D., Horrocks, W. D., Jr., Amburgey, J. C., and Weber, D. J. (1997) *Biochemistry 36*, 9674−9680.
33. Amburgey, J. C., Abildgaard, F., Starich, M. R., Shah, S., Hilt, D. C., and Weber, D. J. (1995) *J. Biomol. NMR 6*, 171−179.
34. Marion, D., Driscoll, P. C., Kay, L. E., Wingfield, P. T., Bax, A., Gronenborn, A. M., and Clore, G. M. (1989) *Biochemistry 28*, 6150−6156.
35. Bax, A., and Ikura, M. (1991) *J. Biomol. NMR 1*, 99−104.
36. Delaglio, F., Grzesiek, S., Vuister, G. W., Zhu, G., Pfeifer, J., and Bax, A. (1995) *J. Biomol. NMR 6*, 277−293.
37. Zhu, G., and Bax, A. (1992) *J. Magn. Reson. 98*, 192−199.
38. Zhu, G., and Bax, A. (1990) *J. Magn. Reson. 90*, 405−410.
39. Edison, A. S., Abildgaard, F., Westler, W. M., Mooberry, E. S., and Markley, J. L. (1994) *Methods Enzymol. 239*, 3−79.
40. Live, D. H., Davis, D. G., Agosta, W. C., and Cowburn, D. (1984) *J. Am. Chem. Soc. 106*, 1939−1941.
41. Spera, S., Ikura, M., and Bax, A. (1991) *J. Biomol. NMR 1*, 155−165.
42. Mori, S., Abeygunawardana, C., Johnson, M. O., and van Zijl, P. C. (1995) *J. Magn. Reson. B 108*, 94−98.
43. Pelton, J. G., Torchia, D. A., Meadow, N. D., and Roseman, S. (1993) *Protein Sci. 2*, 543−558.
44. Ikura, M., Bax, A., Clore, G. M., and Groneborn, A. M. (1990) *J. Am. Chem. Soc. 112*, 9020−9022.

45. Kuboniwa, H., Grzesiek, S., Delaglio, F., and Bax, A. (1994) *J. Biomol. NMR 4*, 871−878.
46. Grzesiek, S., and Bax, A. (1992) *J. Am. Chem. Soc. 114*, 6291−6293.
47. Wittekind, M., and Mueller, L. (1993) *J. Magn. Reson. B 101*, 201−205.
48. Kay, L. E., Ikura, M., Tschudin, R., and Bax, A. (1990) *J. Magn. Reson. 89*, 496−514.
49. Muhandiram, D. R., Guang, Y. X., and Kay, L. E. (1993) *J. Biomol. NMR 3*, 463−470.
50. Bax, A., and Pochapsky, S. S. (1992) *J. Magn. Reson. 99*, 638−643.
51. Christianson, D. W. (1991) *Adv. Protein Chem. 42*, 281−355.
52. Wuthrich, K. (1986) *NMR of proteins and nucleic acids*, John Wiley, New York.
53. Wishart, D. S., and Sykes, B. D. (1994) *J. Biomol. NMR 4*, 171−180.
54. Wishart, D. S., Sykes, B. D., and Richards, F. M. (1992) *Biochemistry 31*, 1647−1651.
55. Rustandi, R. R., Baldisseri, D. M., Drohat, A. C., and Weber, D. J. (1999) *Protein Sci. 8*, 1743−1751.
56. Baudier, J., Labourdette, G., and Gerard, D. (1985) *J. Neurochem. 44*, 76−84.
57. Frederickson, C. J. (1989) *Int. Rev. Neurobiol. 31*, 145−238.
58. Petzold, A., Jenkins, R., Watt, H. C., Green, A. J., Thompson, E. J., Keir, G., Fox, N. C., and Rossor, M. N. (2003) *Neurosci. Lett. 336*, 167−170.
59. Cuajungco, M. P., and Faget, K. Y. (2003) *Brain Res. Brain Res. Rev. 41*, 44−56.
60. Cuajungco, M. P., Faget, K. Y., Huang, X., Tanzi, R. E., and Bush, A. I. (2000) *Ann. N.Y. Acad. Sci. 920*, 292−304.
61. Auld, D. S. (2001) *Biometals 14*, 271−313.
62. Smith, S. P., Barber, K. R., and Shaw, G. S. (1997) *Protein Sci. 6*, 1110−1113.

BI035334Q